Journal of Materials Chemistry A

PAPER

View Article Online
View Journal | View Issue

Check for updates

Cite this: J. Mater. Chem. A, 2019, 7, 6869

Mordant inspired wet-spinning of graphene fibers for high performance flexible supercapacitors†

Nanfei He, [a] Weitao Shan, [b] Julia Wang,[c] Qin Pan, [a] Jiangang Qu, [d] Guofeng Wang [b] and Wei Gao *[a]

Recently, graphene fibers derived from wet-spinning of graphene oxide (GO) dispersions have emerged as viable electrodes for fiber-shaped supercapacitors (FSCs) and/or batteries, wherein large surface area, high electrical conductivity, and sufficient mechanical strength/toughness are desired. However, for most fiber electrodes reported so far, compromises have to be made between energy-storage capacity and mechanical/electrical performance, whereas a graphene fiber with high capacity and sufficient toughness for direct machine weaving or knitting is yet to be developed. Inspired by the alum mordant used for natural dyes in the traditional textile dyeing industry, our research group has synthesized wet-spun GO fibers and coagulated them with different multivalent cations (*e.g.* Ca^{2+}, Fe^{3+}, and Al^{3+}), where dramatically different fiber morphologies and properties have been observed. The first principles density functional theory has been further employed to explain the observed disparities *via* cation–GO binding energy calculation. When assembled into solid-state FSCs, Al^{3+}-based reduced GO (rGO) fibers offer excellent stability against bending, and a specific capacitance of 148.5 mF cm^{-2} at 40 mV s^{-1}, 1.4, 4.8, and 6.8 times higher than that of the rGO fibers based on other three coagulation systems (Fe^{3+}, Ca^{2+} and acetic acid), respectively. The volumetric energy density of the Al^{3+}-based FSC is up to 13.26 mW h cm^{-3}, while a high power density of 250.87 mW cm^{-3} is maintained.

Received 21st December 2018
Accepted 24th February 2019

DOI: 10.1039/c8ta12337c

rsc.li/materials-a

Published on 25 February 2019. Downloaded by University of Pittsburgh on 4/2/2019 9:19:38 PM.

Introduction

Graphene, due to its extraordinary molecular-level properties, such as large surface area, excellent mechanical strength, good optical transparency, and high thermal and electrical conductivities,[1–3] has been extensively studied as an electrode material for electrochemical double-layer capacitors (EDLCs).[4,5] Various macroscopic structures, including one-dimensional (1D) fibers,[6] two-dimensional (2D) films[7] and three-dimensional (3D) frameworks have been assembled.[8] Among these architectures, fiber-shaped supercapacitors (FSCs) have attracted enormous attention, mainly due to their high flexibility which enables them to be manually woven or knitted into fabrics with excellent wearability/breathability, working as energy-storage yarns or fabrics in smart textiles.[9–13] In addition, fiber-shaped energy-storage devices can become attractive power sources for miniaturized electronic devices such as microrobots, physiological sensors, and even implantable medical devices, since they can have small volumes and could be easily transformed into all kinds of shaped structures.[14–16] Moreover, FSC based textiles can be made into multifunctional composites that act as both structural and energy-storage materials, simultaneously. For example, energy-storage textiles can be configured into a solid-state framework as composite structural materials for application in electric vehicles, electric power grids, *etc.*[17,18] The transition of supercapacitors (SCs) into textile fibers addresses a growing technological need for "on-demand" energy in e-textile systems, self-powering miniaturized electronics, multifunctional composites, *etc.*[19]

Solution-processing of graphene oxide (GO) followed by chemical or thermal reduction is a well-established protocol to synthesize large quantities of graphene-like structures.[20] Owing to the abundant oxygen-containing groups (OCGs) on the basal planes and edges, GO can be well dispersed in water. The excellent dispersibility together with its large aspect ratio renders the formation of lyotropic lamellar liquid crystals (LCs) of GO sheets in water with orientational order, enabling their wet spinning into continuous GO fibers,[21] and subsequent reduction of GO (rGO) fibers *via* either chemical or thermal treatments.

[a]Department of Textile Engineering, Chemistry and Science, North Carolina State University, Raleigh, NC 27606, USA. E-mail: wgao5@ncsu.edu

[b]Department of Mechanical Engineering and Materials Science, University of Pittsburgh, Pittsburgh, PA 15261, USA

[c]North Carolina School of Science and Mathematics, Durham, NC 27705, USA

[d]School of Textile and Clothing, Nantong University, 226019, PR China

† Electronic supplementary information (ESI) available: Materials and methods; GO size distribution; SEM images of rGO fibers; DFT calculations; physicochemical properties of the cations; TOF SIMS secondary ion images of rGO fibers; schematic illustration of the wrinkling direction of rGO sheets in each rGO fiber; typical polarized Raman spectra of the rGOF–Al^{3+} fiber and G peak intensity ratios of each rGO fiber; XRD patterns of rGO fibers; equivalent circuit for fitting Nyquist plots and the fitting results; specific capacitance at different current densities of the rGOF–Al^{3+} FSC. See DOI: 10.1039/c8ta12337c

Published on 25 February 2019. Downloaded by University of Pittsburgh on 4/2/2019 9:19:38 PM.

The coagulation bath in the wet-spinning process is one of the most important factors that influences the structures and properties of the as-spun fibers.[22] So far, alkaline baths (such as KOH and NaOH), divalent cations ($CaCl_2$ and $CuSO_4$), positively charged polymer and small molecules (chitosan, CTAB, and diamine), and non-solvents (acetone and glacier acetic acid)[13,23–26] have all been used as coagulants. Among those, insulating polymers or macromolecules will improve the mechanical properties of the resulting fibers but would inevitably compromise the electrical conductivity. In contrast, small metal cations (*e.g.* Ca^{2+}) can diffuse into the as-spun fibers in the wet state, crosslink GO sheets *in situ*, and result in improved mechanical strength and unaffected electrical conductivity of final rGO fibers.[24,27] However, these Ca^{2+} cross-linked fibers are typically made of dense packing of GO/rGO flakes, which is unfavorable for capacitive energy storage.[23] On the other hand, Aboutalebi *et al.*[23] found that rGO fibers from the acetone coagulant generated a more porous structure with a higher specific surface area (SSA), offering higher capacitance over that of the fibers from the Ca^{2+} bath. However, the mechanical and electrical properties of acetone-based rGO fibers were almost one order of magnitude lower than that of the Ca^{2+}-coagulated fibers, mainly due to weak interactions among rGO sheets. Therefore, a trade-off between SSA and mechanical strength/electrical conductivity has to be made for these rGO fibers as supercapacitor electrodes. Hitherto we are still waiting for rGO fibers that can offer excellent energy-storage capability while being compatible with machine weaving and/or knitting.

Historically, mordants (alum/tannin, or aluminium acetate) are widely used in the dyeing industry to improve color efficiency and wash fastness of natural dyes such as Alizarin and Saffron.[28] A mordant is basically a chemical binding reagent that helps the adhesion between polymeric fibers (cotton, silk, and wool) and dye molecules. Traditional mordants used include alum ($AlK(SO_4)_2 \cdot 12H_2O$), cuprous sulfate ($CuSO_4 \cdot 5H_2O$), ferrous sulfate ($FeSO_4$), and aluminum acetate ($Al(OOCCH_3)_3$), all of which are environmentally friendly and cost-effective.[29] To our knowledge, the binding effect of mordants mainly comes from the interactions existing between the multivalent cations and the local chemical moieties in the dye/polymer molecules.[29,30] Also, according to the classic Schulze–Hardy rule,[31,32] the higher valence the cations have, the stronger charge screening the cations can provide. Therefore, trivalent cations (Al^{3+} and Fe^{3+}) are the most widely used inorganic coagulants in wastewater treatment.[33] With regard to GO, trivalent cations, such as Al^{3+}, have been reported to be effective cations for stabilizing GO membranes in water.[34,35] In aqueous dispersions, cations with different charges and electronegativity have different adsorption affinity with GO, leading to transformation and aggregation of GO sheets into various sphere-like flocculation, as reported by Yang *et al.*[36] In addition, trivalent cations have been reported as better cross-linkers for alginate gel than divalent cations for mechanical performance.[37]

GO sheets typically carry various OCGs on their basal planes and the edges, resulting in small sp^2-C domains isolated within the sp^3-C matrix.[38] These functional moieties could offer different interactions with the intercalated ions in between GO sheets, leading to the deformation or corrugation of the GO sheets and thus distinct fiber morphologies.[36] All these interactions are strongly dependent on the intrinsic physicochemical properties of the cation, such as its electron configuration, size, valence number, *etc.* So far, to our knowledge, no report has used trivalent cations as coagulants for wet spinning of GO/rGO fibers. Inspired by the prominent differences brought by the application of trivalent cations in GO membranes, GO dispersions and alginate gels, we have applied trivalent cations in the coagulation process of GO to target enhanced fiber mechanical and morphological features, which are of the primary demands for fiber electrodes in FSC applications.

In our experiment, two types of trivalent metal cations, Al^{3+} and Fe^{3+}, were used as coagulants for rGO fibers (rGOF–Al^{3+} and rGOF–Fe^{3+}) for the first time. In comparison, Ca^{2+} cross-linked and acetic-acid coagulated rGO fibers (rGOF–Ca^{2+} and rGOF–acetic acid) were also prepared as control systems. rGOF–Al^{3+} fibers, owing to their compact and well-aligned structure, offered the highest electrical conductivity, superior to most of the rGO fibers reported in the literature prior to thermal annealing. Meanwhile, trivalent cations, especially Al^{3+}, have led to a more wrinkled fiber morphology with at least 20.5% higher toughness and 4.8 times higher volumetric capacitance, as compared to that of Ca^{2+} and acetic acid coagulated rGO fibers.

Results and discussion

According to the wet-spinning protocol reported in our previous work (Fig. 1),[13] an aqueous dispersion of GO sheets, with an average lateral dimension around 16 μm (Fig. S1†), was extruded into a coagulation bath to form continuous GO fibers at room temperature. The GO sheets can be viewed as a 2D carbon lattice consisting of clustered nano-sp^2 regions and sp^3 carbon matrices.[39] In terms of the coagulation mechanism, the interactions between multivalent metal cations and OCGs on GO sheets are believed to be responsible for the fiber formation and stabilization. In addition, due to the presence of abundant sp^2 clusters, the cation–π interactions between the cations and the π-ring electrons might also play a role in the fiber formation. With the shear stress applied during spinning and the wet-drawing applied during coagulation, GO sheets could be easily aligned along the fiber axis with multivalent cations bridged among them in our processes. The collected as-spun wet-state GO fibers were then washed with DI water to remove physically trapped cations, and then chemically reduced with hydroiodic acid (HI), during which the remaining OCGs were removed and the π-conjugation was partially restored for electrical conductivity.

The SEM images as shown in Fig. 2 and S2† highlight the morphological disparity among the rGO fibers made from different coagulation baths. The trivalent cation (Al^{3+} and Fe^{3+}) coagulated rGO fibers are obviously much more wrinkled with macroscale pores on their surfaces. In comparison, the surfaces of rGO fibers from the divalent cation Ca^{2+} and acetic acid are much smoother with only a few grooves aligned along the fiber axis direction. During the coagulation process, the hydrated

 This journal is © The Royal Society of Chemistry 2019

Published on 25 February 2019. Downloaded by University of Pittsburgh on 4/2/2019 9:19:38 PM.

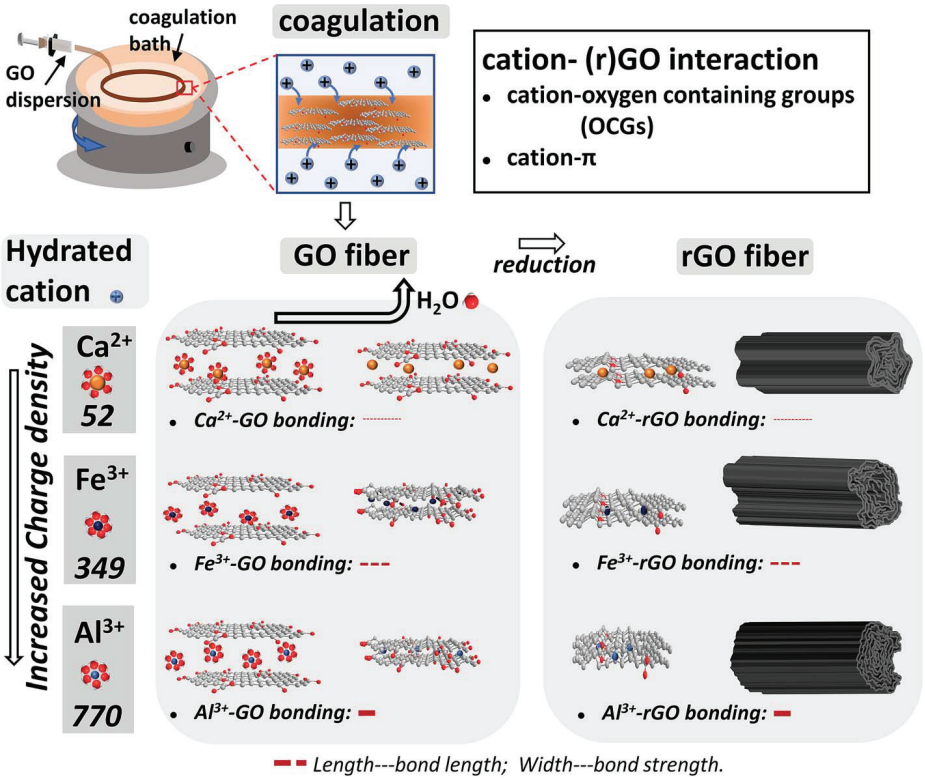

Fig. 1 Schematic illustration of the formation of rGO fibers from divalent and trivalent cations in coagulation baths, respectively. After solvent evaporation and chemical reduction, rGO fibers with different cation cross-linking resulted in dramatically different morphologies.

cations (Al^{3+}, Fe^{3+} or Ca^{2+} ions)[40–42] diffuse into the spaces in between the GO sheets (Fig. 1) and form chemical bonding with the negatively charged OCGs on the GO surfaces. Meanwhile, these multivalent cations can also bind to the aromatic region through cation–π interactions.[35,38] To gain an understanding of the interaction between cations and GO, we have performed the first-principles density functional theory (DFT) calculations (computational details are given in the ESI†) to quantitatively investigate the interaction between cations and OCG abundant regions in GO, which we believe is the primary interaction existing in our system. DFT prediction of the structure and energy of partially hydrated Al^{3+}, Fe^{3+} or Ca^{2+} cations adsorbed on the GO surface was first developed. A 78-atom GO model proposed by Shi–Tu[35,43] and Klinowski[44] *et al.* was used with the formula of $C_{10}O_1(OH)_1$ and with OCGs, which are hydroxyl (–OH) and epoxy (–O–), randomly distributed on both sides of the GO sheet (Fig. S3†). Partial hydration of the cations was modeled as an ion chelated by two –OH groups. Fig. 3a shows the optimized adsorption of the hydrated cations on the GO surface. Our DFT results indicate that the cations prefer to be adsorbed on GO through the formation of ionic bonds with two adjacent epoxy groups at an average bond length of 1.87 Å for Al^{3+}–O, 1.90 Å for Fe^{3+}–O, and 2.38 Å for Ca^{2+}–O. Moreover, our DFT calculation predicted the binding strength of the partially hydrated cations on the GO surface to be 4.39 eV for Al^{3+}, 2.52 eV for Fe^{3+}, and 1.24 eV for Ca^{2+}, respectively. Consequently, our DFT results suggest that hydrated Al^{3+} has the highest tendency to form strong bonding with OCGs followed by Fe^{3+}, whereas hydrated Ca^{2+} has the lowest affinity among the three. Moreover, the DFT method was used to calculate the binding energy between Al, Fe and Ca and the sp^2 carbon region *via* the cation–π interaction (Fig. S4†)[38]. It was predicted that the cation–π interaction with graphene was 0.73 eV for Al, 0.23 eV for Fe, and 0.24 eV for Ca, respectively. Hence, the cation–OCG interaction is dominantly stronger over the cation–π interaction in our DFT models. Meanwhile, the binding strength between the cation and the OCGs really depends on the physicochemical characteristics of the involved cation (Table S1†), where the higher the charge density of the cation, the stronger the cation–OCG interaction.

As interlayer water molecules evaporate during the drying process, the hydration shells of cations shrink gradually. As cations dehydrate (*i.e.*, releasing the two OH groups) and GO sheets approach each other, cations that are intercalated between two GO layers start to bind with two epoxy groups of the other GO layer (Fig. 3b). In this case, the two GO layers are distorted around the intercalated cations, forming large wrinkles and pillars. According to our DFT calculation, it requires 3.97 eV, 2.77 eV, and 2.15 eV activation energy to break such a crosslink formed by Al^{3+}, Fe^{3+}, and Ca^{2+}, respectively. Therefore, the local pinning of the GO layers by Al^{3+} and Fe^{3+} is very difficult to break once it is formed, leading to the corrugated assembly of GO layers. In the case of Ca^{2+}, we believe that its low binding strength on the single layer GO (Fig. 3a) has led to much less adsorption density on the GO surface in the first step. Combined with relatively weak crosslinks between two neighboring GO layers, Ca^{2+} cations favor the formation of face-to-face stacking of GO sheets with less out-of-plane distortion compared to Fe^{3+} and Al^{3+} cations.

Published on 25 February 2019. Downloaded by University of Pittsburgh on 4/2/2019 9:19:38 PM.

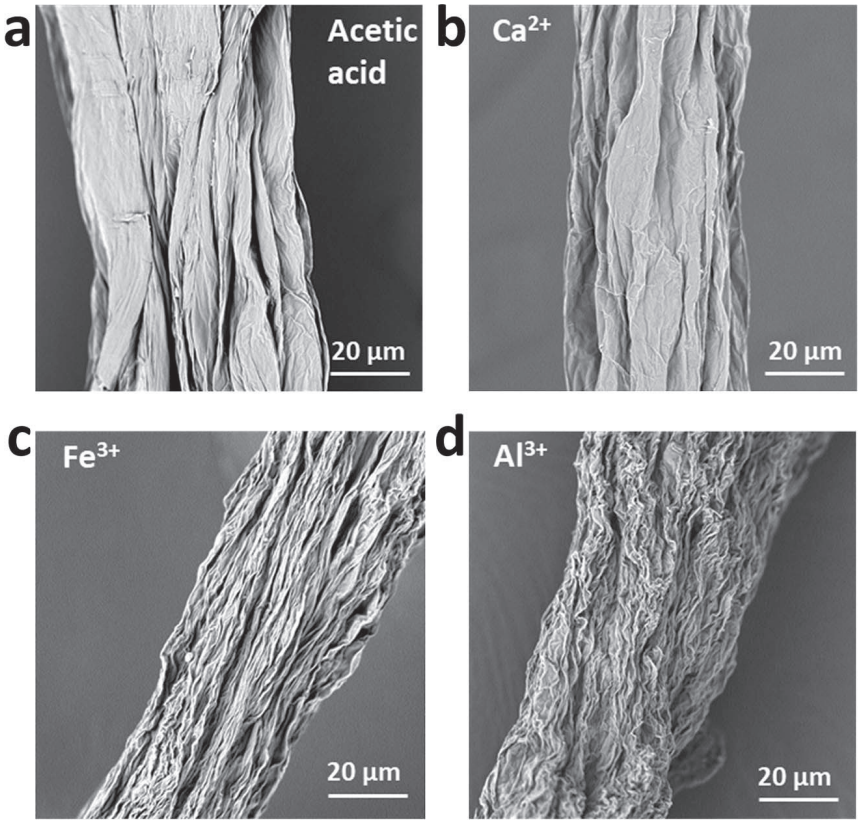

Fig. 2 Morphologies of rGO fibers. SEM images of the (a) acetic-acid coagulated rGO fiber, (b) Ca^{2+} coagulated rGO fiber, (c) Fe^{3+} coagulated rGO fiber, and (d) Al^{3+} coagulated rGO fiber.

After HI reduction, OCGs are partially removed and the graphitic lattice is somewhat restored in rGO fibers. Al^{3+} cations, remaining in the rGO sheet galleries (Fig. S5†), possessing the strongest binding with the residual OCGs and graphitic lattice, give rise to the most buckling structure as observed in rGOF–Al^{3+} (Fig. 2d). Regarding the bulking direction, due to the external force that was applied along the fiber axis during fiber formation, the wrinkles are mostly formed throughout the cross-section of rGO fibers and perpendicular to the fiber axis (Fig. S6†). Meanwhile, along the fiber axis, most of the rGO sheets have less prominent wrinkles and still maintain a high level of orientation (calculation details are given in the ESI, Fig. S7 and Table S2†). From XRD patterns, Ca^{2+} cations with a large radius lead to interrupted sheet stacking and broad XRD signals (Fig. S8†). Because of the relatively smaller radius of Al^{3+}, rGOF–Al^{3+} has a narrower peak with a slightly lower inter-sheet spacing of 0.375 nm, as compared to that of rGOF–Ca^{2+} (0.377 nm). Comparing among trivalent cations, Fe^{3+} with lower charge density possesses a weaker interaction with rGO sheets, resulting in a less compact structure with a larger interlayer spacing (0.382 nm) (Fig. S5†) than that of rGOF–Al^{3+}. The SSA measurement results through methylene blue (MB) adsorption are (Table 1) in agreement with the morphological observations of rGO fibers. The rGOF–Al^{3+} gives the highest value of 685.8 $m^2\ g^{-1}$, ~14% higher than that of rGOF–Fe^{3+} (601.1 $m^2\ g^{-1}$) and ~51% higher than that of rGOF–Ca^{3+} (454.7 $m^2\ g^{-1}$) and rGOF–acetic acid (445.9 $m^2\ g^{-1}$).

Representative stress–strain curves of rGO fibers are depicted in Fig. 4a and the mechanical properties along with the electrical conductivities of rGO fibers are summarized and

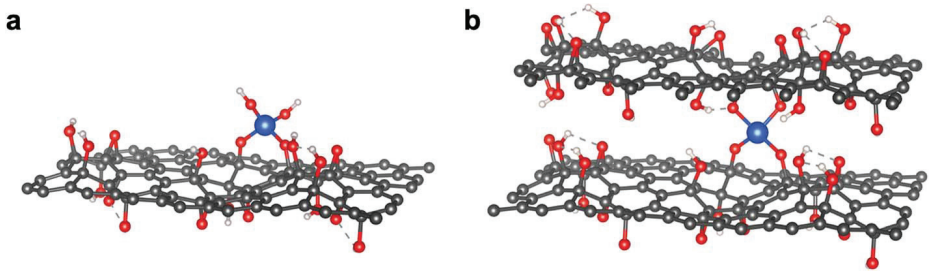

Fig. 3 Atomic structures of hydrated cation adsorption on a single layer GO surface (a) and intercalated atoms between two GO layers (b). In the figure, the black, red, white, and blue balls represent carbon, oxygen, hydrogen, and cations (Al^{3+}, Fe^{3+}, or Ca^{2+}), respectively.

 This journal is © The Royal Society of Chemistry 2019

Published on 25 February 2019. Downloaded by University of Pittsburgh on 4/2/2019 9:19:38 PM.

Table 1 Mechanical and electrical properties of rGO fibers

Sample	SSA/m^2 g^{-1}	Tensile strength/MPa	Breaking elongation/%	Toughness/MJ m^{-3}	Electrical conductivity/S cm^{-1}
rGO–Al^{3+}	685.8	164.9 ± 2.1	10.3 ± 2.1	10.0 ± 2.1	171.3 ± 9.1
rGO–Fe^{3+}	601.1	154.7 ± 5.5	11.2 ± 3.5	8.7 ± 2.5	110.6 ± 5.7
rGO–Ca^{2+}	454.7	240.9 ± 32.5	6.2 ± 0.9	8.3 ± 1.2	128.0 ± 6.2
rGO–acetic acid	445.9	145.6 ± 11.8	6.9 ± 0.8	4.1 ± 0.8	85.7 ± 0.9

compared in Table 1. It is evident that the composition of the coagulation bath significantly influences the mechanical properties of the resulting rGO fibers. As expected, rGO fibers prepared by ionic cross-linking displayed higher tensile strength and toughness as compared to the fibers from the non-solvent coagulation bath (acetic acid) where the cross-linking effect is absent. For rGO fibers coagulated from acetic acid, the lateral cohesion of adjacent rGO sheets can be assigned as van der Waals interactions as well as some residual hydrogen-bonding. For fibers coagulated from metal cations, in addition to van der Waals interactions, the interaction between cations with residual OCGs and aromatic planes also contributes to the improvement of the fiber mechanical performance.

Generally, Al^{3+} and Fe^{3+} cross-linked fibers exhibited medium tensile strength, but larger breaking elongation, resulting in higher toughness than that of Ca^{2+} and acetic acid coagulated fibers. Specifically, rGOF–Al^{3+} has a tensile strength of 164.9 ± 2.1 MPa at a breaking elongation of 10.3 ± 2.1%, resulting in a toughness value of 10.0 ± 2.1 MJ m^{-3}, 20.5%, and 144.6% higher than that of rGOF–Ca^{2+} and rGOF–acetic acid. High toughness against fracture under tensile stress indicates good flexibility which is favorable for textile processing, such as twisting, weaving and knitting. The toughness of rGO fibers can be divided into two parts, *i.e.* the strain energy stored in the in-plane tensile deformation of rGO sheets and the one in the shear deformation of interlayer crosslinks.[45] As compared to divalent Ca^{2+} and acetic acid coagulated rGO fibers, Al^{3+} and Fe^{3+} coagulated fibers have more wrinkled rGO sheets along the fiber axis, which can contribute more to the in-plane tensile deformation. Within rGO fibers coagulated from trivalent ions, rGOF–Al^{3+} with a more compact structure exhibits higher tensile strength and slightly lower breaking strain as compared to rGOF–Fe^{3+} with a larger layer spacing.

The electrical conductivity of rGO fibers was measured by the four-probe method (Fig. 4b inset) rather than the two-probe method, mainly to eliminate the effect of contact resistance

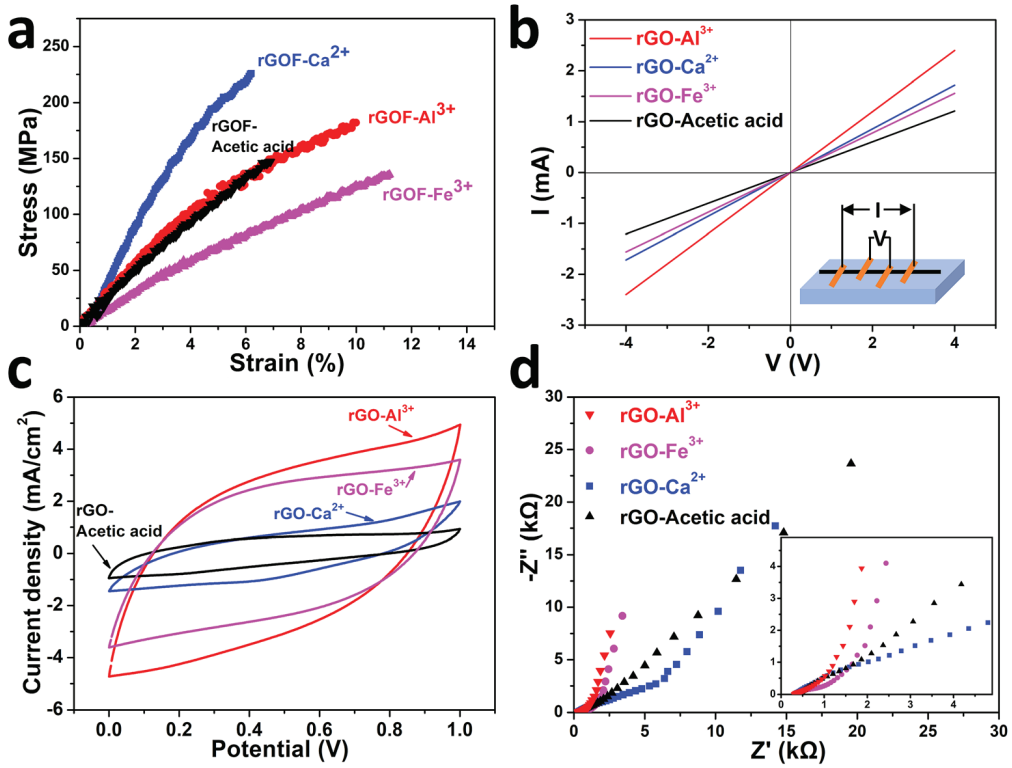

Fig. 4 Comparison of the mechanical, electrical and electrochemical properties of rGO fibers coagulated from trivalent cation baths (Al^{3+} and Fe^{3+}), divalent cation baths (Ca^{2+}), and non-crosslinker acetic acid. (a) Representative stress–strain curves of rGO fibers prepared using various coagulation baths. (b) Typical *I*–*V* curves of rGO fibers with the length of 2 cm. The inset shows a schematic of our four-probe apparatus for the electrical conductivity measurements. (c) CV curves at 40 mV s^{-1}. (d) Nyquist plot from the EIS test.

Published on 25 February 2019. Downloaded by University of Pittsburgh on 4/2/2019 9:19:38 PM.

that originates from the contacting interfaces of electrical leads and connections.[46] Fig. 4b shows the typical *I–V* curves of these rGO fibers. The rGOF–Al^{3+} shows the highest electrical conductivity (171.3 ± 9.1 S cm^{-1}) in comparison with other rGO fibers, mainly due to its compact structure and well-aligned rGO sheets along the fiber axis. The capacitive performance of these rGO fibers is mainly ascribed to double-layer capacitance, which is proportional to the electrolyte accessible surface area. rGO fibers coagulated from various chemicals were assembled into symmetrical parallel FSCs and evaluated based on their cyclic voltammogram (CV) responses at 40 mV s^{-1} (Fig. 4c). All FSCs showed a quasi-rectangular CV curve representative of good double-layer formation. Obviously, fibers coagulated from trivalent ions exhibited much higher capacitance. For example, the rGOF–Al^{3+} FSC exhibited a capacitance of 148.5 mF cm^{-2} (213.7 F cm^{-3}), ~4.8 times and 6.8 times higher than that of rGOF–Ca^{2+} and rGOF–acetic acid based FSCs, respectively. This originated from the more wrinkled surfaces of trivalent cation-crosslinked rGO fibers as observed in Fig. 2, offering a much larger accessible area to electrolyte, and favoring the diffusion and adsorption of electrolyte ions.

In addition, electrochemical impedance spectroscopy (EIS) characterization was applied to evaluate the equivalent series resistance (ESR) of all the FSCs. Fig. 4d shows the Nyquist plot with frequency ranging from 0.01 Hz to 0.1 MHz with an amplitude of 10 mV which is analyzed using the equivalent circuit model (Fig. S9†). As presented in this model, R_s is the series resistance, which is related to both the electron conductivity and ion mobility.[47] Since the same electrolyte used in all these FSCs, the R_s is in the same sequence as that of the electrical conductivity of the corresponding fiber electrode. The charge transfer resistance (R_{ct}) represents faradaic processes at the electrode and electrolyte interfaces. All the FSC systems here are absent of a semicircle in the high frequency region, indicating that there is negligible R_{ct} between the electrolyte and electrodes. Warburg impedance (W_0) is associated with the diffusion of electrolyte ions within electrodes. CPE_{dl} represents the straight line, parallel to the imaginary axis in the Nyquist plots at lower frequency, and it is proportional to the capacitance of these FSCs. As we can see, FSCs assembled from trivalent ion coagulated fibers have an obviously shorter Warburg region (lower W_0), indicating better ion transport in the porous network. The shorter and more vertical line at the lower frequency domain implies a larger double layer capacitance in trivalent ion fibers. Accordingly, trivalent ion coagulated fibers exhibited much better EDLC performance compared to the other rGO fibers. For comparison among trivalent ion coagulated fibers, rGOF–Al^{3+} exhibited 28% larger specific capacitance and 20% lower ESR than that of rGOF–Fe^{3+}, mainly owing to the higher electrical conductivity of rGOF–Al^{3+}.

To fully understand the performance of the solid-state rGOF–Al^{3+} assembled FSC, we characterized its electrochemical behavior using CV and galvanostatic charge/

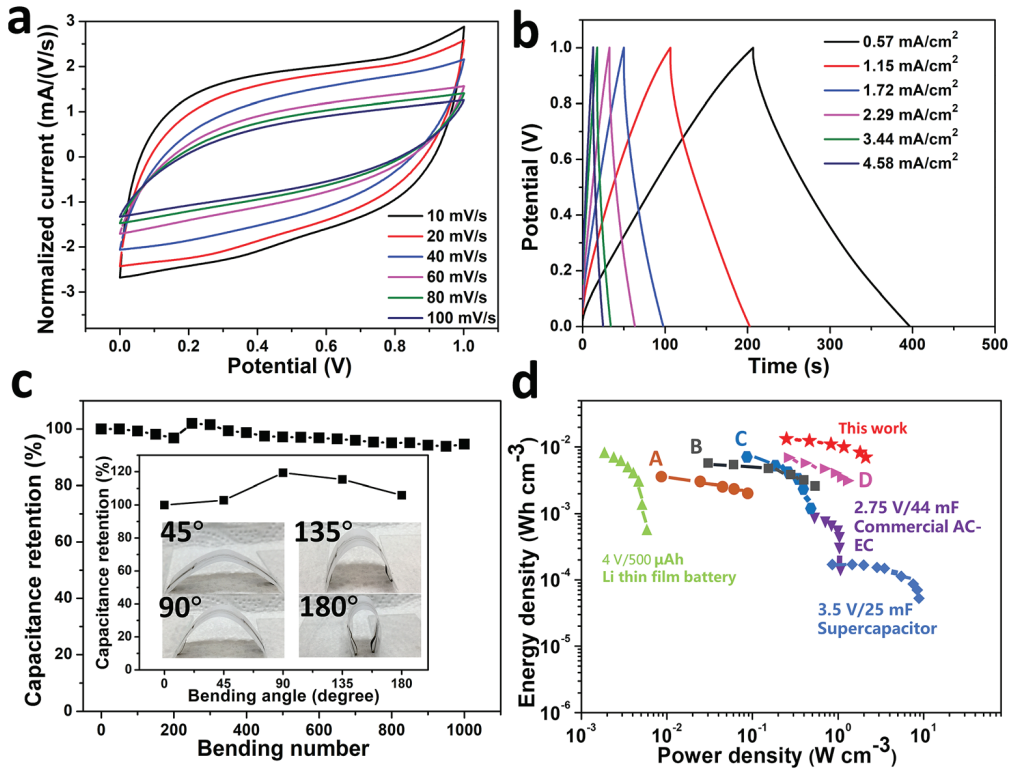

Fig. 5 Electrochemical characterization of the rGOF–Al^{3+} FSC in PVA/H_2SO_4 electrolyte. (a) CV curves at different scan rates and (b) galvanostatic charge/discharge curves at different current densities. (c) Capacitance retention as a function of bending cycles, the inset is capacitance stability upon bending from 0° to 180°. (d) Ragone plot of the rGOF–Al^{3+} FSC compared with some commercial devices and other reported FSCs, including the commercially available 4 V/500 μA h Li thin-film battery,[48] 3.5 V/25 mF SC,[49] 2.75 V/44 mF commercial AC-EC[50] and (A) hierarchically porous sheath–core graphene based FSC,[51] (B) rGO/cellulose hybrid FSC,[52] (C) non-LC spinning pure rGO FSC,[53] and (D) rGO@NMP-FSC.[13]

 This journal is © The Royal Society of Chemistry 2019

Published on 25 February 2019. Downloaded by University of Pittsburgh on 4/2/2019 9:19:38 PM.

discharge (GCD) measurements. As shown by the CV curves at different scan rates in Fig. 5a, the FSC almost presents a quasi-rectangular shape and can maintain its shape at the scan rate of 100 mV s^{-1}. The GCD curves exhibit nearly linear symmetrical shapes with a coulombic efficiency of ~94%, implying the good reversibility of the FSC and good charge propagation between two rGOF–Al^{3+} electrodes (Fig. 5b). The specific area capacitance of the rGOF–Al^{3+} FSC calculated from the discharge curve is shown in Fig. S10.† Clearly, the rGOF–Al^{3+} FSC displays a large specific capacitance of 286.59 mF cm^{-2} at a current density of 0.53 mA cm^{-2}. When the current density increases to as high as 10.62 mA cm^{-2}, the specific capacitance decreased to 106.51 mF cm^{-2}. This capacitance decay at high current density was most likely due to the insufficient ionic transport in the charge/discharge process.

The fiber-shaped solid-state FSC does not require additional packaging, exhibiting high flexibility, and is robust enough to undergo one thousand bending cycles, which is a key requirement for wearable electronics applications. We measured the capacitance retention of the FSC under various bending angles (0°, 45°, 90°, 135° and 180°) (Fig. 5c inset). An improved capacitance is observed upon bending and it peaked at 90° (improved by 19%). This improvement might be due to the enhancement of electrolyte penetration within the unfolded wrinkles in the stretched region. In addition, high bending durability is observed with less than 10% decrease in capacitance after 1000 bending cycles at the 180° bending angle (Fig. 5c).

The volumetric energy density (E_V) and power density (P_V) of the FSCs are more meaningful parameters for evaluating the energy-storage performance of the device. Fig. 5d presents the Ragone plot of the rGOF–Al^{3+} FSC, showing its E_V and P_V compared with other FSC systems and commercially available film batteries and supercapacitors, all data here were normalized without packaging. It can be seen that the E_V and P_V of our rGOF–Al^{3+} FSCs are at the upper corner of the Ragone plot. The E_V of the rGOF–Al^{3+} (based on the device) is up to 13.26 mW h cm^{-3} at the current density of 0.71 A cm^{-3} (corresponding to a power density of 250.87 mW cm^{-3}), better than that of the 2.75 V/44 mF commercial activated carbon (AC)-electrochemical capacitor (EC) (0.7 mW h cm^{-3} at 590 mW cm^{-3}),[50] and 3.5 V/25 mF SC,[49] and higher than that of the 4 V/500 μA h Li thin-film battery (0.3–10 mW h cm^{-3}).[48] Moreover, this value also outperforms those of the recently reported various graphene and carbon fiber based FSCs (Table S4†), such as the hierarchically porous sheath–core graphene based FSC (2–3.4 mW h cm^{-3}),[51] rGO/cellulose hybrid FSC (5.1 mW h cm^{-3} at 30.7 mW cm^{-3}),[52] non-LC spinning pure rGO FSC (7.03 mW h cm^{-3} at 57.7 mW cm^{-3}),[53] and our previous work: a FSC assembled from the pure wet-spun rGO fiber originating from the NMP based spinning dope (rGO@NMP-FSC) (6.8 mW h cm^{-3} at 120.4 mW cm^{-3}).[13] The maximum volumetric power density of our rGOF–Al^{3+} FSC was as high as 2109 mW cm^{-3} at the current density of 5.7 A cm^{-3}, holding an obvious advantage over most of the reported systems.

Conclusions

In summary, we have demonstrated the use of Al^{3+} cations as a novel coagulant in the wet-spinning of GO/rGO fibers, which leads to higher toughness, superior electrical conductivity, and improved capacitance density of the resulting rGO fibers as compared to that of other rGO fibers. As a trivalent cross-linker for GO fibers, Al^{3+} has an advantage over divalent cations (*e.g.* Ca^{2+}) in terms of generating much more wrinkled morphologies in the fibers, which facilitate the adsorption and diffusion of electrolyte ions. DFT modeling results have indicated the highest binding energy of Al^{3+} among the three cations with GO, providing a reasonable explanation for high wrinkling resulted in the Al^{3+}-based fibers. When compared to Fe^{3+} cations, Al^{3+} cations with much larger charge density lead to a more compact structure, and thus stronger and more conductive rGO fibers. The specific area capacitance of solid-state FSCs assembled with rGOF–Al^{3+} was up to 148.5 mF cm^{-2} at 40 mV s^{-1}, 1.4, 4.8 and 6.8 times higher than that of FSCs from rGOF–Fe^{3+}, rGOF–Ca^{2+} and rGOF–acetic acid, respectively. It also shows excellent stability upon bending at various angles and good long-term bending durability. Furthermore, the maximum energy density of 13.26 mW h cm^{-3} at 0.71 A cm^{-3} and the maximum power density of 2109 mW cm^{-3} at 5.7 A cm^{-3} of rGOF–Al^{3+} FSC are much higher than those of the reported rGO and carbon based FSCs. The investigation of trivalent ions as coagulation reagents for wet-spun GO fibers has shed light on the design and fabrication of conductive, flexible and high surface area rGO fibers for application in wearable technologies.

Conflicts of interest

The authors declare no competing financial interests.

Acknowledgements

This work was financially supported by the start-up and FRPD funding of Dr Gao's group in the Textile Engineering, Chemistry and Science Department at North Carolina State University, as well as the grant from US Department of Defense with grant number W911NF18C0086. W. Shan and G. Wang acknowledge research grants from the National Science Foundation (Grant No. CBET-1804534 and CMMI-1662615), and the computational resources provided by the University of Pittsburgh Center for Research Computing as well as the Extreme Science and Engineering Discovery Environment (XSEDE), which is supported by the National Science Foundation grant number ACI-1053575.

References

1 X. Du, I. Skachko, A. Barker and E. Y. Andrei, *Nat. Nanotechnol.*, 2008, **3**, 491–495.
2 C. Lee, X. D. Wei, J. W. Kysar and J. Hone, *Science*, 2008, **321**, 385–388.
3 J. H. Seol, I. Jo, A. L. Moore, L. Lindsay, Z. H. Aitken, M. T. Pettes, X. S. Li, Z. Yao, R. Huang, D. Broido, N. Mingo, R. S. Ruoff and L. Shi, *Science*, 2010, **328**, 213–216.

Published on 25 February 2019. Downloaded by University of Pittsburgh on 4/2/2019 9:19:38 PM.

4 M. D. Stoller, S. Park, Y. Zhu, J. An and R. S. Ruoff, *Nano Lett.*, 2008, **8**, 3498–3502.
5 C. Liu, Z. Yu, D. Neff, A. Zhamu and B. Z. Jang, *Nano Lett.*, 2010, **10**, 4863–4868.
6 Y. J. Liu, Z. Xu, W. W. Gao, Z. D. Cheng and C. Gao, *Adv. Mater.*, 2017, **29**, 1606794.
7 H. A. Becerril, J. Mao, Z. Liu, R. M. Stoltenberg, Z. Bao and Y. Chen, *ACS Nano*, 2008, **2**, 463–470.
8 J. Li, J. Li, H. Meng, S. Xie, B. Zhang, L. Li, H. Ma, J. Zhang and M. Yu, *J. Mater. Chem. A*, 2014, **2**, 2934–2941.
9 Z. Xu and C. Gao, *Mater. Today*, 2015, **18**, 480–492.
10 S. Seyedin, E. R. S. Yanza and J. Razal, *J. Mater. Chem. A*, 2017, **5**, 24076–24082.
11 L. Lim, Y. Liu, W. Liu, R. Tjandra, L. Rasenthiram, Z. Chen and A. Yu, *ACS Appl. Mater. Interfaces*, 2017, **9**, 39576–39583.
12 B. Li, J. Cheng, Z. Wang, Y. Li, W. Ni and B. Wang, *J. Power Sources*, 2018, **376**, 117–124.
13 N. He, Q. Pan, Y. Liu and W. Gao, *ACS Appl. Mater. Interfaces*, 2017, **9**, 24568–24576.
14 F. Soavi, L. G. Bettini, P. Piseri, P. Milani, C. Santoro, P. Atanassov and C. Arbizzani, *J. Power Sources*, 2016, **326**, 717–725.
15 L. Li, Z. Lou, D. Chen, K. Jiang, W. Han and G. Shen, *Small*, 2018, **14**, 1702829.
16 D. Yu, Q. Qian, L. Wei, W. Jiang, K. Goh, J. Wei, J. Zhang and Y. Chen, *Chem. Soc. Rev.*, 2015, **44**, 647–662.
17 N. Muralidharan, E. Teblum, A. S. Westover, D. Schauben, A. Itzhak, M. Muallem, G. D. Nessim and C. L. Pint, *Sci. Rep.*, 2018, **8**, 17662.
18 C. Meng, N. Muralidharan, E. Teblum, K. E. Moyer, G. D. Nessim and C. L. Pint, *Nano Lett.*, 2018, **18**, 7761–7768.
19 S. W. Pan, J. Ren, X. Fang and H. S. Peng, *Adv. Energy Mater.*, 2016, **6**, 1501867.
20 H. P. Cong, J. F. Chen and S. H. Yu, *Chem. Soc. Rev.*, 2014, **43**, 7295–7325.
21 Z. Xu and C. Gao, *Nat. Commun.*, 2011, **2**, 571.
22 J. Chen, C. G. Wang, X. G. Dong and H. Z. Liu, *J. Polym. Res.*, 2006, **13**, 515–519.
23 S. H. Aboutalebi, R. Jalili, D. Esrafilzadeh, M. Salari, Z. Gholamvand, S. A. Yamini, K. Konstantinov, R. L. Shepherd, J. Chen, S. E. Moulton, P. C. Innis, A. I. Minett, J. M. Razal and G. G. Wallace, *ACS Nano*, 2014, **8**, 2456–2466.
24 Z. Xu, H. Y. Sun, X. L. Zhao and C. Gao, *Adv. Mater.*, 2013, **25**, 188–193.
25 H. P. Cong, X. C. Ren, P. Wang and S. H. Yu, *Sci. Rep.*, 2012, **2**, 613.
26 Y. S. Kim, J. H. Kang, T. Kim, Y. Jung, K. Lee, J. Y. Oh, J. Park and C. R. Park, *Chem. Mater.*, 2014, **26**, 5549–5555.
27 R. Jalili, S. H. Aboutalebi, D. Esrafilzadeh, R. L. Shepherd, J. Chen, S. Aminorroaya-Yamini, K. Konstantinov, A. I. Minett, J. M. Razal and G. G. Wallace, *Adv. Funct. Mater.*, 2013, **23**, 5345–5354.
28 A. K. Samanta and P. Agarwal, *Indian J. Fibre Text. Res.*, 2009, **34**, 384–399.
29 G. Mock, *Lecture Notebook*, College of Textiles, NCSU, 1997.
30 A. Ajmal and P. R. Piergiovanni, *Ind. Eng. Chem. Res.*, 2018, **57**, 4462–4469.
31 J. T. G. Overbeek, The Rule of Schulze and Hardy, *Pure Appl. Chem.*, 1980, **52**, 1151.
32 M. Sano, J. Okamura and S. Shinkai, *Langmuir*, 2001, **17**, 7172–7173.
33 W. Nowicki and G. Nowicka, *J. Chem. Educ.*, 1994, **71**, 624.
34 C. N. Yeh, K. Raidongia, J. J. Shao, Q. H. Yang and J. X. Huang, *Nat. Chem.*, 2015, **7**, 166–170.
35 L. Chen, G. Shi, J. Shen, B. Peng, B. Zhang, Y. Wang, F. Bian, J. Wang, D. Li, Z. Qian, G. Xu, G. Liu, J. Zeng, L. Zhang, Y. Yang, G. Zhou, M. Wu, W. Jin, J. Li and H. Fang, *Nature*, 2017, **550**, 380.
36 K. Yang, B. Chen, X. Zhu and B. Xing, *Environ. Sci. Technol.*, 2016, **50**, 11066–11075.
37 C. H. Yang, M. X. Wang, H. Haider, J. H. Yang, J. Y. Sun, Y. M. Chen, J. X. Zhou and Z. G. Suo, *ACS Appl. Mater. Interfaces*, 2013, **5**, 10418–10422.
38 P. Sun, F. Zheng, M. Zhu, Z. Song, K. Wang, M. Zhong, D. Wu, R. B. Little, Z. Xu and H. Zhu, *ACS Nano*, 2014, **8**, 850–859.
39 P. Sun, H. Liu, K. Wang, M. Zhong, D. Wu and H. Zhu, *J. Phys. Chem. C*, 2014, **118**, 19396–19401.
40 X. L. Lei and B. C. Pan, *J. Phys. Chem. A*, 2010, **114**, 7595–7603.
41 M. F. Bush, R. J. Saykally and E. R. Williams, *ChemPhysChem*, 2007, **8**, 2245–2253.
42 I. Persson, *Pure Appl. Chem.*, 2010, **82**, 1901–1917.
43 J. Yang, G. Shi, Y. Tu and H. Fang, *Angew. Chem., Int. Ed.*, 2014, **53**, 10190–10194.
44 H. He, J. Klinowski, M. Forster and A. Lerf, *Chem. Phys. Lett.*, 1998, **287**, 53–56.
45 Y. Liu, B. Xie, Z. Zhang, Q. Zheng and Z. Xu, *J. Mech. Phys. Solids*, 2012, **60**, 591–605.
46 T. Ebbesen, H. Lezec, H. Hiura, J. Bennett, H. Ghaemi and T. Thio, *Nature*, 1996, **382**, 54–56.
47 N. He, O. Yildiz, Q. Pan, J. Zhu, X. Zhang, P. D. Bradford and W. Gao, *J. Power Sources*, 2017, **343**, 492–501.
48 D. Pech, M. Brunet, H. Durou, P. Huang, V. Mochalin, Y. Gogotsi, P.-L. Taberna and P. Simon, *Nat. Nanotechnol.*, 2010, **5**, 651.
49 L. Liu, Y. Yu, C. Yan, K. Li and Z. Zheng, *Nat. Commun.*, 2015, **6**, 7260.
50 M. F. El-Kady, V. Strong, S. Dubin and R. B. Kaner, *Science*, 2012, **335**, 1326–1330.
51 X. Zheng, K. Zhang, L. Yao, Y. Qiu and S. Wang, *J. Mater. Chem. A*, 2018, **6**, 896–907.
52 G. Chen, T. Chen, K. Hou, W. Ma, M. Tebyetekerwa, Y. Cheng, W. Weng and M. Zhu, *Carbon*, 2018, **127**, 218–227.
53 S. Chen, W. Ma, Y. Cheng, Z. Weng, B. Sun, L. Wang, W. Chen, F. Li, M. Zhu and H.-M. Cheng, *Nano Energy*, 2015, **15**, 642–653.

 This journal is © The Royal Society of Chemistry 2019